Design of MIMO Planar Sparse Array and Improved Back-Projection Algorithm for High-Performance 3-D Microwave Imaging

Zhengyue Dong, Yuke He, Kuiwen Xu, Shaoqing Hu, Qinyi Lv, Xiaokang Qi, Xuetiao Ma, Xiaotong Li, Chao Sun, Jiangtao Su, Wenjun Li

Abstract—A novel two-step iterative optimization method could be used in microwave and mm-wave bands for optimal topology of 2-D sparse multiple input multiple output (MIMO) arrays and an improved back-projection algorithm (IBPA) for near-range scenarios have been proposed to achieve high-resolution three-dimensional (3D) imaging. According to point spread functions (PSF), the array topology results from the proposed design method has superior performance on sidelobe level both in the interference region (IR) and non-interference region (NIR), and the obtained peak sidelobe levels (PSLs) are lower than the conventional topologies over 2 dB. The IBPA has weighting factors incorporated into its forward physical wave equations to improve accuracy of the model. The imaging capabilities of the proposed array and IBPA have been experimentally verified. The proposed array could further mitigate the artifact distribution in target image than conventional arrays which is consistent to theoretical analysis. The proposed IBPA could provide higher resolution and lower PSLs without increasing the computational complexity.

Index Terms—Multiple-input-multiple-output (MIMO) array, optimization methods, 2-D sparse array, sidelobes suppression, improved BPA.

I. INTRODUCTION

Two-dimensional (2-D) array-based ultrawideband (UWB) MIMO microwave imaging techniques have been widely applied in various applications, such as remote sensing [1], airport security [2][3], through-the-wall imaging (TWI) and rescue [4][5], ground-penetrating radar imaging (GPR) [6][7], nondestructive testing [8-10], and medical diagnosis [11-13].

The state-of-the-art imaging systems are capable of achieving real-time high-resolution 3-D imaging, while facing the

compromise among the imaging accuracy, computational burden, and system costs [14-15]. In those imaging systems, the element spacing within the synthetic 2-D aperture should not be more than one-half wavelength (even a quarter wavelength in near-field scenarios) in order to prevent unexpected grating lobes. That is to say, the conventional uniform 2-D array systems not only bring in high hardware costs but also introduce the unavoidable mutual coupling issue. Hence, significant efforts have been made in investigating the capabilities of 2-D sparse arrays.
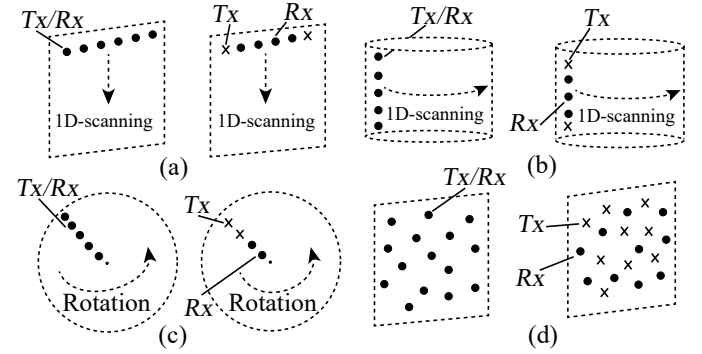

Fig. 1. Typical 2-D array topologies. (a) 1-D linear array with 1-D scanning. (b) 1-D linear array with cylindrical scanning. (c) 1-D linear array with radial scanning. (d) 2-D real aperture array.

A 2-D sparse array could be virtually synthesized by moving a 1-D sparse linear array in space or achieved by constructing a 2-D real aperture sparse array. The scanning strategies with 1-D linear array and topologies of 2-D real aperture array are illustrated in Fig. 1. 2-D Sparse array imaging systems could reduce the hardware cost and data acquisition time while providing high-resolution reconstruction images. Whereas, the overlapped spectrum caused by under-sampling data would result in grating lobes in the reconstruction images [16][17]. To circumvent the problem, 2-D sparse arrays were proposed by using signals with large bandwidth. Hence, the level of grating lobes could be reduced for 2-D sparse array imaging systems when the fractional bandwidth is much larger [18-22]. Although the large operational bandwidth could suppress the grating lobes to some extent, it brings a heavy burden for designing hardware sub-systems with a large operational bandwidth.

To further suppress the grating lobes and also to reduce the number of antennas, microwave imaging systems are devel-

oped with 2-D sparse MIMO array, in which the transmitters and receivers are spatially separated to synthesize a larger effective aperture in two cross-range directions. Hence, the number of antenna elements and data-acquisition time could be significantly reduced without degrading image quality [23-25]. Although the MIMO technique enables superior imaging capabilities, the performance of 2-D sparse MIMO arrays is greatly impacted by both the operational bandwidth and topologies of arrays and MIMO technique with large operational bandwidth should be utilized to develop 2-D sparse array imaging systems. The grating lobes level of these MIMO arrays could be analyzed and calculated through the theory of effective element [26-27]. However, an optimal 2-D MIMO array topology could not be obtained conveniently. Significant efforts have been made to realize the optimization topologies of MIMO array. For example, by arranging antenna distributions according to Fermat's spiral geometries, a 2-D curvilinear array is developed [28]. In [29], an extended optimal MIMO array (EOA) with the number of transmitter and receiver elements being integral multiples of 4 is obtained through the 'Grid' method. To improve the compatibility of 2-D MIMO arrays design method, an optimization method based on compressive sensing is used to obtain both positions and weighting factors of the elements [30]. Besides, an extended coherence factor (ECF) method based on the sub-band sub-aperture (SBSA) data is utilized to combat side/grating lobes and simultaneously overcome insufficient data [19]. Then, the multi-apodization (MA) method and pixel search (PS) method are used to cut off the shifted grating-lobes while maintaining the resolution [20]. Although the strategies above could suppress grating lobes to some extent, they are only suitable for some particular scenarios such as the number of transceivers being integral multiples of 4. A more general design principle for designing a 2-D sparse MIMO array with any number of elements in a customized aperture is not reported to our best knowledge.

Herein, a two-step iterative method for the design of 2-D MIMO array with lower grating lobes for 3-D microwave imaging is proposed and an improved back-projection algorithm for sidelobes suppression which is applicable to arbitrary topology configurations is used. The contributions of this work could be summarized as follows:

1) A two-step iterative method is proposed for the microwave and millimeter-wave bands, where the positions of transceivers are optimized to obtain the optimal topology of the corresponding 2D MIMO array. The optimization method could be applicable to any number of transceivers in a customized aperture size.

2) An improved back-projection algorithm for sidelobes suppression is accordingly proposed for near-field imaging scenarios. In the physical model of IBPA, novel weighting factors have been incorporated into the forward wave equations to improve the accuracy of model.

3) Theory analysis, numerical simulation and measurement have verified that the proposed IBPA has better imaging performance compared to conventional BP in grating/side-lobes, distributed targets reconstruction capabilities and cross-range resolution in the IR region.
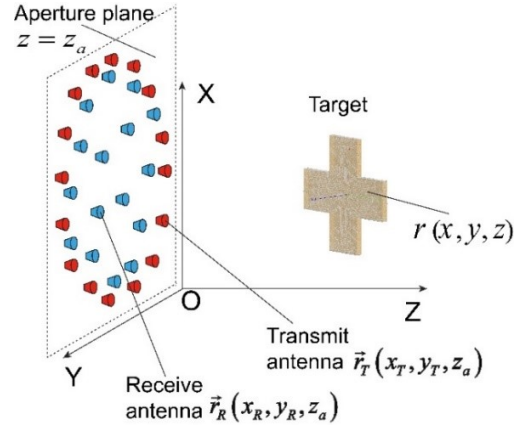

Fig. 2. Illustration of 2-D planar MIMO imaging system in near-range scenarios.

II. DESIGN PRINCIPLES OF 2-D SPARSE MIMO ARRAY

A. Configuration of MIMO Imaging System

The configuration of imaging system based on the 2-D sparse MIMO array is shown in Fig. 2. Transmitters and receivers are sparsely distributed in a flat plane $z = z_a$, while the object under test is located in front of the 2-D array within the domain of interest (DoI) bounded by the field of view of imaging system. The position of transmitter element is $\overrightarrow{r_T}(x_T, y_T, z_a)$, and the position of the receiver element is $\overrightarrow{r_R}(x_R, y_R, z_a)$. A general point at $r(x, y, z)$ in the DoI is characterized by a reflectivity function $f(x, y, z)$. In a forward problem with Born approximation and neglecting the multiple scattering inside the targets, the received signals denoted as $S(x_T, y_T, x_R, y_R, k)$, could be summarized as [30],

$$S(x_T, y_T, x_R, y_R, k) = p(k) \cdot \iiint_V f(x, y, z) dx dy dz$$
$$\times e^{(-jk(r_T + r_R))} \tag{1}$$

$$r_T = \sqrt{(x - x_T)^2 + (y - y_T)^2 + (z - z_a)^2} \tag{2}$$

$$r_R = \sqrt{(x - x_R)^2 + (y - y_R)^2 + (z - z_a)^2} \tag{3}$$

where $p(k)$ is the wideband signal radiated from the transmitters. r_T and r_R are the distances between the point in DoI and transmitter element, receive element, respectively. Inversely, reflectivity function of the distributed target within the DoI, namely, $f(x, y, z)$ could be accordingly reconstructed as,

$$f(x, y, z) = \iint \iiint \frac{1}{p(k)} dx_T dy_T dx_R dy_R dk$$
$$\times S(x_T, y_T, x_R, y_R, k) \times e^{jk(r_T)} e^{jk(r_R)} \tag{4}$$

where $k = w/c$ (c is the speed of the propagation and w is the temporal angular frequency) is the wavenumber.

B. Topology Design

As discussed in [31-35] for a 1-D MIMO array design, both the weighting factors and distribution of effective elements

$$E_{AP} = \left\{ (r_{Emn}, w(r_{Emn})) \Big|_{w(r_{Emn}) = w_{Tx}(r_{Tm}) \cdot w_{Rx}(r_{Rn})}^{r_{Emn} = |r_{Tm} + r_{Rn}|} \right\} \tag{5}$$

will determine the level and spatial distribution of grating/side-lobes. The level of grating/side-lobes of a 2-D MIMO array could be evaluated by transforming them into its effective array according to the projection-slice method [26-27]. In this way, the strategies utilized to design 1-D MIMO arrays could be a useful tool to optimize the topology of the corresponding 2-D array. The effective aperture of MIMO array could be obtained by [26-27]

where $m=1,...,N_t$; $n=1,...,N_r$, and N_t and N_r are the total number of transmitter elements and receiver elements, respectively. w_{Tx} and w_{Rx} denote weighting factor of an antenna element within the transmitter and receiver apertures. r_{Tm} and r_{Rn} represent the mth elements in the transmitter aperture and nth receiver aperture. It is noted that when the different transceiver pairs within the aperture result in the same virtual element position r_{Emn}, the weighting factors of these effective elements should be summed up together as $\sum w(r_{Emn})$.

According to the projection slice method [26-27], the projection of effective array elements r_{Emn} onto a rotated axis at a certain angle determines the array pattern at that specific angular cut. According to [26] [31-33], it can be concluded that the array would obtain the greatest performance when the effective elements r_{Emn} of a MIMO array are uniformly distributed in each rotated axis and the corresponding weighting factors $w(r_{Emn})$ of these elements are exactly the same in each axis. Furthermore, the dynamic range of 2-D arrays possessing N elements within E_{AP} can be evaluated by the following two equations [27],

$$ISL = 20\log_{10}\left(\frac{1}{N}\right) \tag{6}$$

$$PSL = 20\log_{10}\left(\max(w(r_{Emn}))/\sum_{n=1}^{N} w(r_{Emn})\right) \tag{7}$$

where ISL and PSL are the ideal sidelobe level and the peak sidelobe level, respectively. N is the total number of effective elements r_{Emn}. N is equal to the total number of array elements within E_{AP} for a MIMO array, that is, $N = N_t \cdot N_r$.

C. Degree of Freedom

The values of PSL would approach ISL when the projection of elements $r_E mn$ have a unit weighting. The values of PSL and ISL are desired to be close to each other for achieving better imaging performance. Hence, the degree of free (DoF) for the transmitter and receiver antennas could be defined as,

$$DoF = \min_{(r_{Tm}, r_{Rn})} ||PSL - ISL||_2 \tag{8}$$

the low DoF would lead to a lower grating/side-lobes level.

In order to realize the best performance with a constant number of antennas, two efficient design principles as follows should be complied with:

Principle 1: The effective elements r_{Emn} should be uniformly distributed within the whole effective aperture E_{AP} with as little redundancy as possible. It is noted that the spacing of the elements is much less than the pulses width, i.e., $\bar{d} < T/2$ (where T is pulse width) would be regarded as redundant ones. In this way, the imaging systems have satisfying performance around the main-lobe area whether the measured objects are located at the center or the edge of the effective aperture E_{AP}[26].

Principle 2: The projection of effective array elements r_{Emn} onto a rotated axis at each angular cut should be uniformly distributed and keep the equivalent line array with almost the same weighting factor.

D. Optimization Principles

Based on above principles, a two-step iterative method is proposed to optimize the position of the transmitter and receiver elements sequentially. The flow chart of the optimization procedures is shown in Fig. 3, including three steps.

1) Step 1: Calculate Configuration Parameters

According to the requirements of the imaging system, the number of effective antennas N could be calculated with (6) and (7). And the effective aperture size, Δ_{EAP} could be estimated by the azimuth, height, and range mean resolution,$\delta_a, \delta_h, \delta_r$, respectively, using the formulas below [26][29][31].

$$\delta_a \approx \frac{\lambda_c}{(2\Delta_{EAP})} R_a \tag{9}$$

$$\delta_h \approx \frac{\lambda_c}{(2\Delta_{EAP})} R_h \tag{10}$$

$$\delta_r = \frac{c}{2 \cdot B} \tag{11}$$

where λ_c, R_a and R_h are the wavelength corresponding to the center frequency, the aperture size in the azimuth direction, and the aperture size in the height direction, respectively. c and B represent the speed of light and the system's operating bandwidth.

The resolution over the whole imaging region is not a constant value which could be analyzed through 3D spatial frequency components. The resolution within ROI has a complicated relationship with the position distribution of the transceiver elements. To simplify the analysis procedure, the formulas (9)-(11) have been utilized to quickly evaluate the level of the resolution.

2) Step 2: Optimization of the Receiver Elements

To meet above principles, the positions of the receiver elements should be optimized firstly. The transmitter elements should be located in a circle with a radius slightly larger than Δ_{EAP}, whereas the receiver elements should be distributed

inside the region bounded by the aperture Δ_{EAP}. To reduce the mutual-coupling between the elements and meet the requirement of Principle 2 along both horizontal and vertical projection directions, the positions of receiver elements could be expressed by,

$$r_R = \left\{ (x_{Rn}, y_{Rn}) \left| \begin{matrix} x_{Rn} \in s \\ y_{Rn} \in s \end{matrix} \right. \right\} \quad (12)$$

where the domain s is a linear space vector

$$s = [-l\frac{\Delta_r}{N_r} : \frac{\Delta_r}{N_r} : l\frac{\Delta_r}{N_r}] \quad (13)$$

and $l = (N_R - 1)/2$. The receiver aperture size Δ_r could be approximated empirically by,

$$\Delta_r = \Delta_{EAP} - 0.02 * \Delta_{EAP}. \quad (14)$$

Herein, the different receivers have various coordinates, meaning that $x_{Ri} \neq x_{Rj}$ and $y_{Ri} \neq y_{Rj}$. In this case, PSL could approach ISL in horizontal and vertical axis. Then the positions of receiver elements need to be changed to acquire the best result in all possible combinations satisfying (10) and (11). To estimate the effective covering area of the designed antennas, the Voronoi diagram is defined [36]. The area of the Voronoi cell could be calculated and the uniformity index (UI) is defined as the maximum area of the Voronoi cell minus the minimum area of the Voronoi unit.

$$UI = \min_{(r_{Rn})} (Svo_{\max} - Svo_{\min}) \quad (15)$$

where $S_{vo_{max}}$ and $S_{vo_{min}}$ are maximum area of the cell and minimum area of another cell in the Voronoi diagram.

The procedures of optimizing receivers are summarized in Fig. 4. With initial positions r_{Rn} of receiver elements, the UI
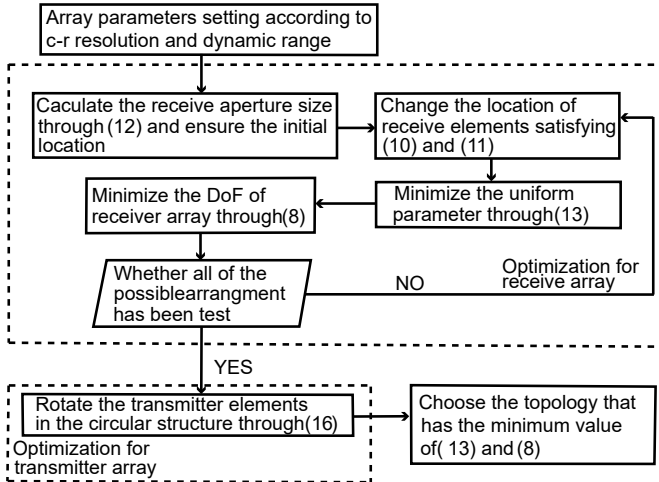

Fig. 3. Flow chart of the two-step optimization method.

is calculated and PSL is calculated from $0°$ to $360°$ to evaluate the maximum grating/side-lobes in each angular direction with a step of $1°$. The array topology with both minimization values of (8) and (13) has the greatest sidelobe control capabilities both in the IR and the NIR regions.
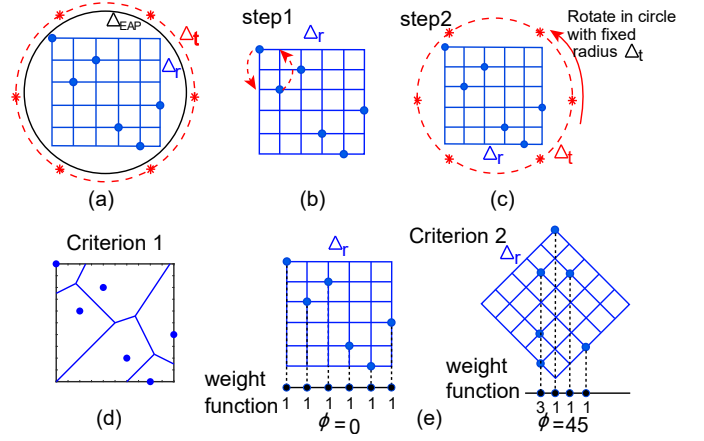
3) Step 3: Optimization of the Transmitter Elements

Fig. 4. Illustration of the two-step iterative optimization method. (a) The quantification process of equivalent aperture, transmitter and receiver aperture. (b) Optimization process of (b) receiver elements and (c) transmitter elements. (d) Illustration of Principle 1. (e) Illustration of Principle 2.

Based on step 2, to achieve a uniform distribution of the virtual array, the transmitter elements should be placed in a circle owing to its rotationally symmetrical properties. Then, the transmitter aperture size Δ_T is expressed by,

$$\Delta_T = \Delta_{EAP} - 0.035 * \Delta_{EAP} \quad (16)$$

The transmitter elements are in a circle with the radius of $\Delta_T/2$ and the positions could be obtained by,

$$r_T = \left\{ (x_{Tm}, y_{Tm}) \left| \begin{matrix} x_{Tm} = \Delta_T/2 \cdot cos(2 \cdot \pi \cdot n/N_t) \\ y_{Tm} = \Delta_T/2 \cdot sin(2 \cdot \pi \cdot n/N_r) \end{matrix} \right. \right\} \quad (17)$$

Due to the spareness of transmitter elements, the projection of transmitter elements onto the slices is highly different among various angular cuts. To obtain the optimal positions for transmitter elements, they should be rotated and the rotated positions could be given by,

$$\begin{bmatrix} x_{Tm}^{(i)} \\ y_{Tm}^{(i)} \end{bmatrix} = \begin{bmatrix} \cos\theta^{(i-1)} & \sin\theta^{(i-1)} \\ -\sin\theta^{(i-1)} & \cos\theta^{(i-1)} \end{bmatrix} \cdot \begin{bmatrix} x_{Tm} \\ y_{Tm} \end{bmatrix} \quad (18)$$

The values of θ are ranging from 0 to 360 degrees with a step of one degree. Following the optimization procedures for the receivers, the optimal position of transmitter elements, namely, $(x_{Tm}^{(i)}, y_{Tm}^{(i)})$, could be finally obtained when (8) and (13) are satisfied within all possible combinations $(x_{Tm}^{(i)}, y_{Tm}^{(i)}), r_R n$. Through above procedures, the optimal topology of MIMO array, (r_{Tm}, r_{Rn}), could be obtained.

III. IMPROVED BACK-PROPAGATION ALGORITHM

Under the first-order Born approximation, the receiving field $S(x_T, y_T, x_R, y_R, k)$ of the conventional BP could be expressed by [29],

$$S(x_T, y_T, x_R, y_R, k) = p(k) \iiint_V f(x, y, z) \cdot \frac{e^{-jk(r_T + r_R)}}{16\pi^2 r_T r_R}$$

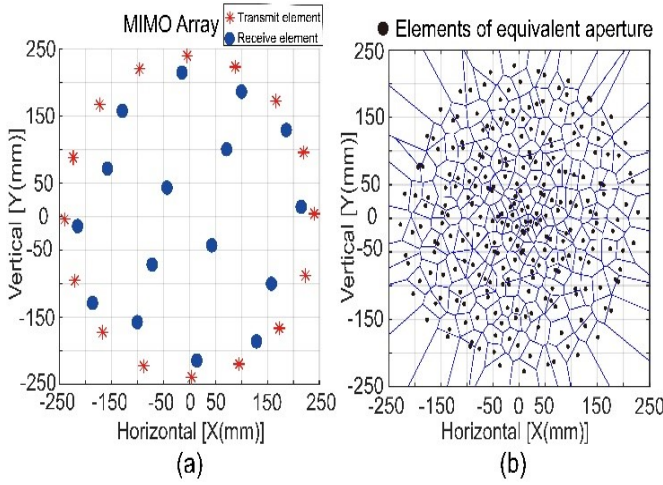$$\times w_T(x - x_T, y - y_T) w_R(x - x_R, y - y_R) dx dy dz \quad (19)$$

Fig. 5. MIMO array and its corresponding Voronoi cells (a) 2-D sparse MIMO array. (b) Voronoi cells of the virtual array.

Fig. 6. Illustration of sparse MIMO array imaging system. Apertures S_0,S_1,and unit vectors n_1, n_2 are shown intuitively.

where w_T,w_R are the weighting factors brought by the radiation patterns with respect to the corresponding transceiver elements. Finally, the image could be reconstructed by [29],

$$f(x,y,z) = \iiint \frac{S(x_T,y_T,x_R,y_R,k)}{p(k) \cdot w_t(x - x_T, y - y_T)}$$

$$\frac{e^{jk(r_T+r_R)} \cdot 16\pi^2 r_T r_R}{w_r(x - x_R, y - y_R)} \times dx_T dy_T dx_R dy_R dk \qquad (20)$$

where weighting factors w_T, w_R are calculated through narrowing the gap between the imaging response of a point-like scatterer and the desired reference pattern [30].

Herein, an improved back-projection algorithm (IBPA) for sidelobes suppression by use of a novel strategy has been proposed to quantify the weight factors with a significant improvement in focusing capabilities and PSL levels.

The Voronoi cells of the corresponding virtual elements of the 2-D sparse MIMO array are shown in Fig. 5(b). Based on ERM (exploration reflector model) [36], some algorithms in time domain have illustrated different weighting factors for the imaging application of sparse MIMO arrays [37] [38]. However, the weighting factors used in time domain has shed some light on the inversion method of frequency domain. Accordingly, the weighting factors of the corresponding transceiver pairs could be expressed as,

$$w(r_{Emn}) = S_{vo} \cdot \frac{\partial r_T}{\partial n_1} \cdot \frac{\partial r_R}{\partial n_2} \cdot \frac{1}{r_T r_R} \qquad (21)$$

where S_0 and S_1 represent the transmitter and receiver apertures, n_1 is the unit normal to S_0, n_2 is the unit normal to S_1. S_{vo} is the Voronoi area of corresponding transceiver pairs. The illustration of (19) is expressed in Fig. 6. $\frac{\partial r_T}{\partial n_1}, \frac{\partial r_R}{\partial n_2}$ denote the vectors of partial derivatives, perpendicular to the closed surface formed by the receiver array aperture and transmitter array aperture, respectively.
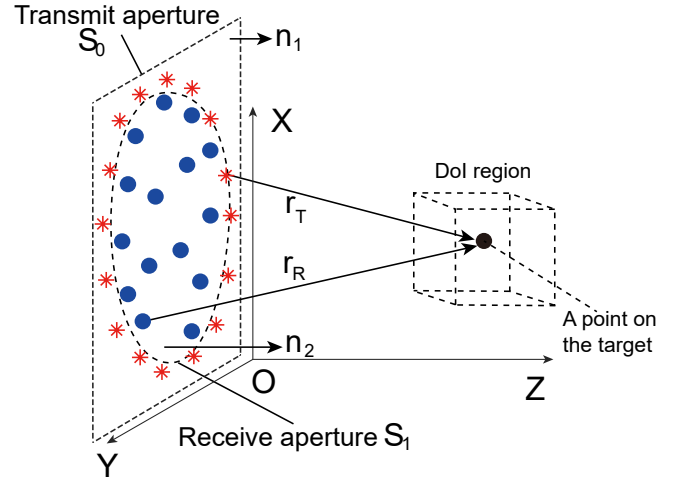
TABLE I
COMPARISON OF COMPUTATIONAL COMPLEXITY

Algorithm	Computational Complexity
BPA	$N_u N_v N_x N_y N_z N_k + N_u N_v N_k$ $+ N_u N_v N_x N_y$
IBPA	$N_u N_v N_x N_y N_z N_k + N_u N_v N_k$ $+ N_u N_v$

Then, the inverse procedure of IBPA could be solved by,

$$f(x,y,z) = \iiint_{S_0 S_1} w(r_{Emn}) \cdot \frac{S(x_T,y_T,x_R,y_R,k)}{p(k) \cdot r_T r_R}$$

$$\times e^{jk(r_T+r_R)} \times dS_0 dS_1 dk \qquad (22)$$

Assuming that the number of discrete points in the azimuth, range, and elevation directions in the ROI area are N_x, N_y, and N_z, respectively. The number of elements in the transmitting aperture and the receiving aperture are N_u and N_v, respectively. The number of samples in the frequency domain is N_k. The computational complexity of these could be summarized as shown in Table I. It could be observed that under the same systems conditions, the computational complexity of the IBPA is slightly lower than that of the BPA.

IV. NUMERICAL SIMULATION AND RESULTS

A. Design of 2-D Sparse MIMO Arrays

To verify the proposed principles, we apply them to design 2-D sparse MIMO arrays and evaluate their imaging performance theoretically and experimentally. Herein, 3-D images reconstruction ability is required for the imaging system with a down-range resolution of 15 mm and a cross-range resolution of 30 mm at the range of 500 mm.

The proposed MIMO array is shown in Fig. 7(d). It is noted that the distance of two elements $\bar{d}$ should be large

TABLE II
IMAGING PERFORMANCE OF MIMO ARRAYS FOR POINT TARGETS

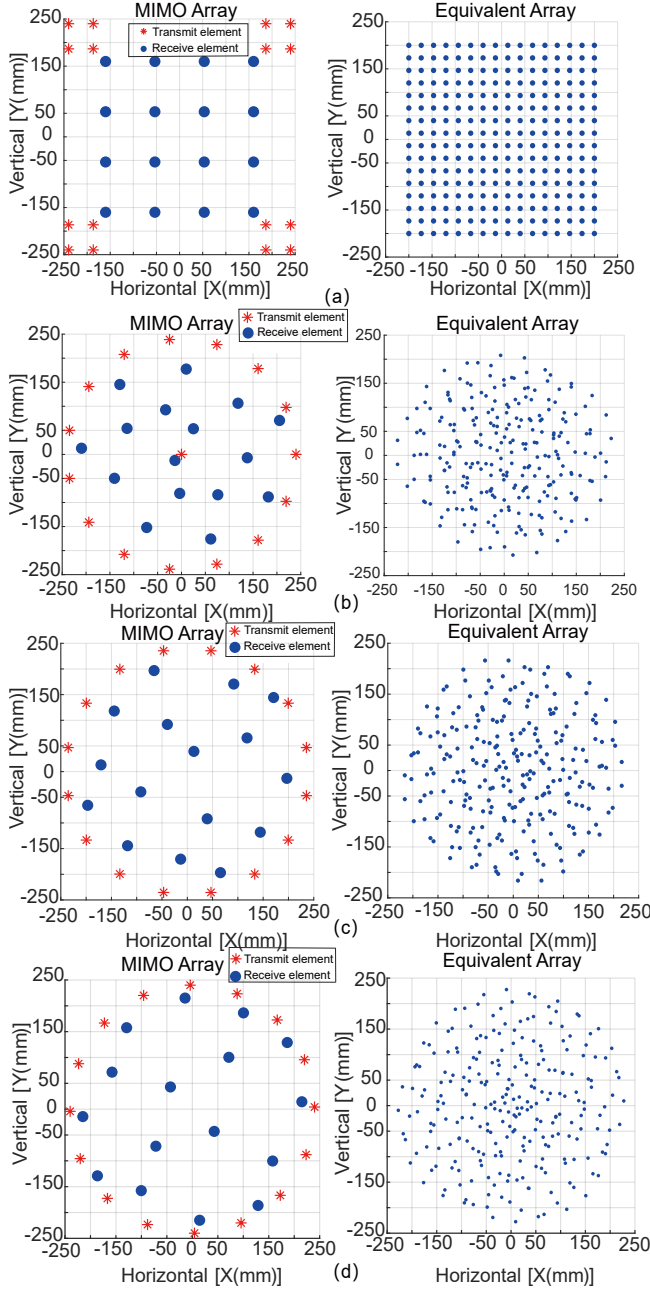| 2-D MIMO Arrays	$\max(w(r_{Emn}))$	Theoretical PSL (dB)	Simulated PSL (dB)	UI (m²)	3-dB Beamwidth (cm)
Proposed Array	12	-26.58	-23.63	0.0013	1.436
Curvilinear Array	14	-25.24	-22.04	0.0025	1.622
EOA Array	13	-25.88	-22.31	0.0015	1.448
Square Array	16	-24.08	-19.59	0.0008	1.216

Fig. 7. MIMO array topologies and their corresponding equivalent array apertures. (a) Equivalent uniform rectangular array (Array I). (b) Curvilinear structure composed array (Array II). (c) Extent optimal MIMO array (EOA) (Array III). (d) Proposed array (Array IV).
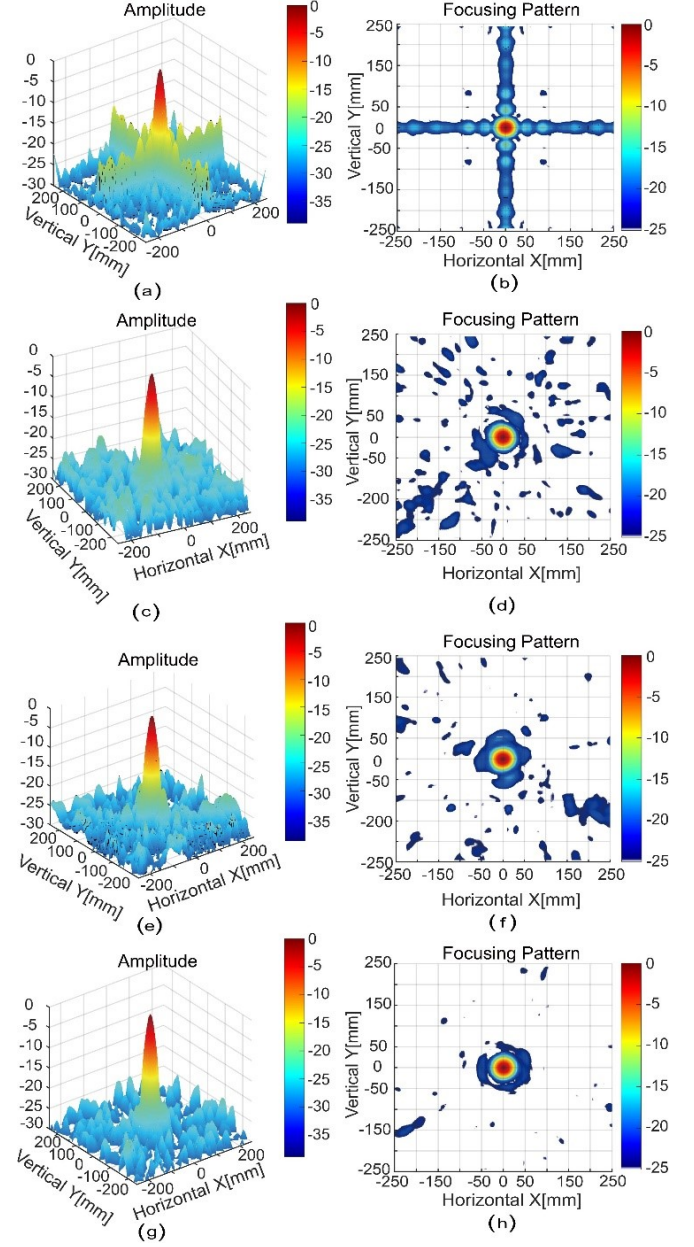
Fig. 8. Radiation patterns of MIMO arrays in Fig. 7 with a focal point at $(0,0,20\lambda_c)$. (a) Pattern of array I (b) Top view of (a). (c) Pattern of array II. (d) Top view of (c). (e) Pattern of array III. (f) Top view of (e). (g) Pattern of array IV. (h) Top view of (g).
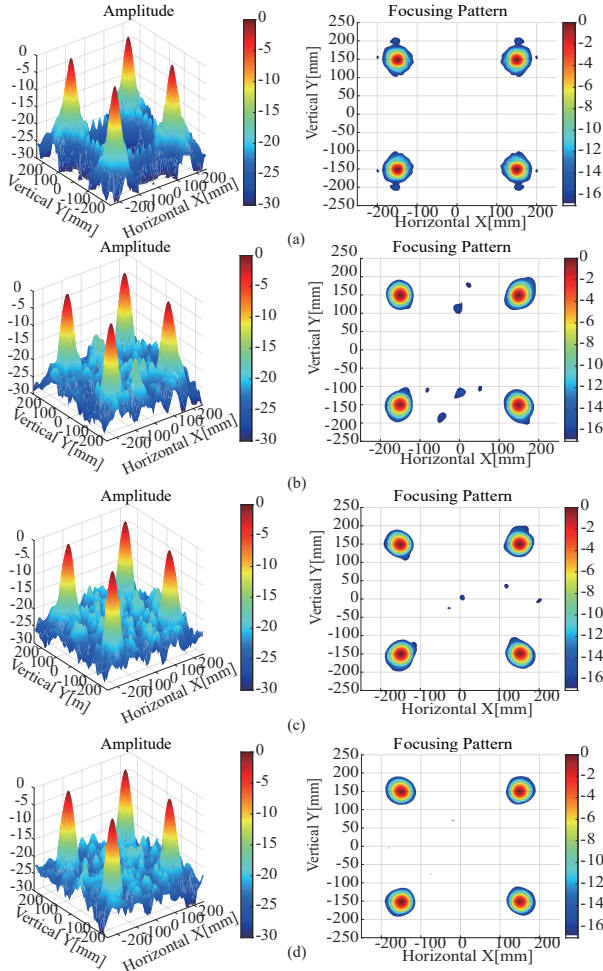
Fig. 9. Imaging results of MIMO arrays for point targets located at the edge position($\pm5\lambda_c,\pm5\lambda_c,20\lambda_c$). (a) Equivalent uniform rectangular array (Array I). (b) Curvilinear structure composed array(Array II). (c) Extent optimal MIMO array(EOA) (Array III). (d) Proposed array (Array IV).

than pulses length, which in our study refers to the time-domain duration of the transmitted signal,in order to maintain the sparseness of the MIMO arrays and reduce the mutual-element-coupling. Hence, under the conditions of the required cross-range resolution, the size of the effective aperture, E_{AP}, should be no less than 0.5 m×0.5 m according to (9). The center frequency is 10 GHz, and the operation frequencies are ranging from 5 to 15 GHz (100% fraction bandwidth).

The proposed MIMO array has 32 elements with 16 transmitter and 16 receiver elements. The transmitter antennas are distributed in a circular structure with a radius of 240mm. The optimal positions of receiver elements could be obtained through the procedures of the first dashed box parts in Fig. 3. It is compared with a widely used MIMO topology and two previous start-of-the-art topologies shown in Fig. 7(a), (b) and (c) as references, namely the equivalent uniform rectangular array [39] (Array I), the curvilinear MIMO array [28] (Array II), and the extended optimal MIMO array (EOA) (Array III) [29]. The equivalent virtual array elements of array I are uniformly distributed but exhibit high periodicity. Hence, the elements shadowing would appear along 0°, 90°, 45°,

135°, and the highest values of PSL would appear along the orthogonal plane of those directions. The equivalent virtual array elements of array II and III are randomly distributed which means the number of overlapping elements is reduced greatly. Therefore, they will exhibit better angular properties compared to array I. In contrast, the proposed array (array IV) has been optimized through the optimization procedures. It strictly meets the above principles, so overlapping elements could be reduced furtherly. The values of UI and PSL of those MIMO arrays are summarized in Table II. It could be concluded that the proposed array has the lowest PSL value and the best angular resolution compared to others.

TABLE III
IMAGING PERFORMANCE OF MIMO ARRAYS FOR POINT
TARGETS IN EDGE REGION

2-D MIMO Arrays	FC (dB)	PSL (dB)
Array	7.13	-17.17
Curvilinear Array	8.38	-14.86
EOA Array	7.56	-16.57
Square Array	10.77	-14.95

B. Simulation of Point Targets

In the simulation, Hertzian dipoles are used as both transmitter and receiver elements for optimizing array topology. They are computationally cheaper, making them suitable for the preliminary validation of the array design. After background subtraction, the optimized array topology could also be suitable for Vivaldi antenna cases. The array positions and operating frequency band in the simulation are based on our previous array design and the actual system. For a single-round simulation, which refers to a complete simulation of the entire array, the process is carried out by choosing one antenna as the transmitter and the remaining 16 as receivers, iterating through all 16 transmitter antennas in turn. The time required using Hertzian dipoles as the simulation element is significantly less compared to using Vivaldi antenna. Therefore, for efficient array optimization, employing the Hertzian dipoles is a more reasonable approach in terms of the time costs and effectiveness. A 1.5-cm-diameter metallic sphere is used as a point target in front of the center of the array at a range of $20\lambda_c$ distance. λ_c is the operating wavelength of 10 GHz, which is 3 cm. Results of imaging a point scatterer using the above 2-D sparse MIMO arrays have been compared in Fig. 8 reconstructed by the conventional back-propagation method [29]. It shows that the sidelobes could be well suppressed for the Array IV while the other arrays exhibit high sidelobes, which is consistent with the above theoretical analysis.

The proposed array demonstrates enhanced uniformity and significantly reduced element shadowing across all projection axes. As a result, it aligns more closely with Principle 1 and Principle 2's design principles than other arrays. This improved design leads to lower sidelobe levels and a more uniform artifact distribution throughout the imaging space.
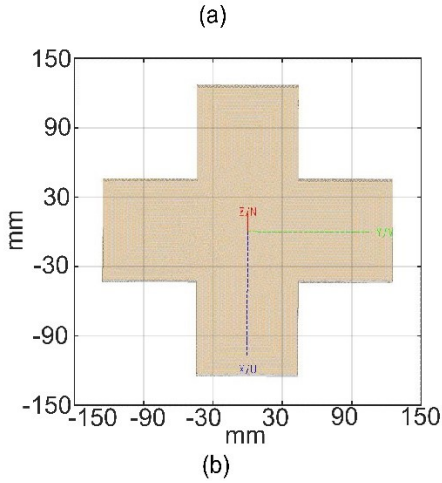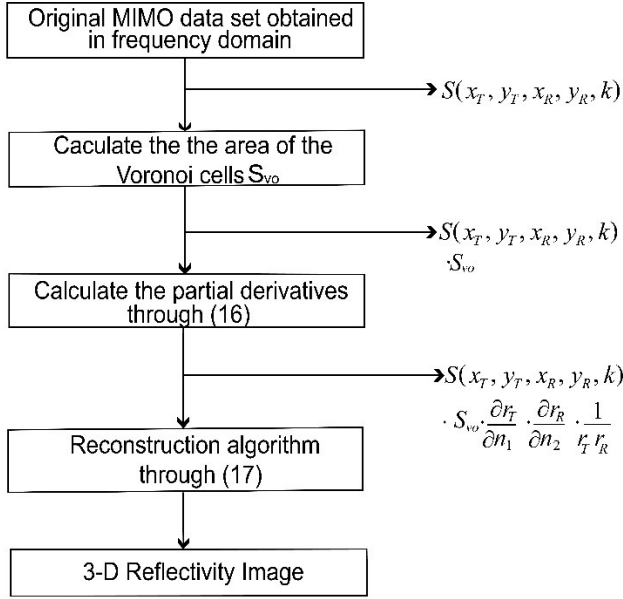
Fig. 10. (a) Procedures of IBPA. S_{vo} is the area of Voronoi cells within the effective array while $\frac{\partial r_T}{\partial n_1} \cdot \frac{\partial r_R}{\partial n_2} \cdot \frac{1}{r_T r_R}$ is the weighting factors used in the ERM model in time-domain analysis. (b) Testing object in FEKO.

Fig. 11. 3-D reconstructions of distributed target and their front views under -15-dB level. (a) 2-D and 3-D images obtained by array I. (b) 2-D and 3-D images obtained by array II. (c) 2-D and 3-D images obtained by array III. (d) 2-D and 3-D images obtained by array IV

Consequently, its imaging performance is theoretically superior to that of other arrays. Our results also confirm this improved performance.

The simulation results of PSL values and its corresponding 3-dB beamwidth of MIMO arrays are summarized in Table II. It could be seen that the simulated PSL values are slightly higher than theoretical ones owing to the mutual-coupling effect among elements. The proposed array has the lowest PSL of -23.63 dB.

In addition, to illustrate that our array has advantages, we give the imaging results of the edge region in Fig. 9 and Table IV. It could be seen that in the NIR region, the proposed array has the lowest PSL of -17.17 dB and best FC of 7.13.

C. Simulation of Distributed Targets

To further verify imaging capabilities of the MIMO arrays in Fig. 7., simulations for distributed targets have been carried

TABLE IV
QUANTITATIVE IMAGING PARAMETERS
FOR DISTRIBUTED TARGETS

2-D MIMO Arrays	FC (dB)	PSL (dB)
Array	7.19	-12.74
Curvilinear Array	11.24	-9.44
EOA Array	7.26	-11.77
Square Array	12.22	-10.6

out. The distributed object is a cross-shape object which is made of PEC as shown in Fig. 10(b). The reconstructed results are summarized in Fig. 11(a) and (b) show sightly deformations in the IR region, which could be caused by strong effect
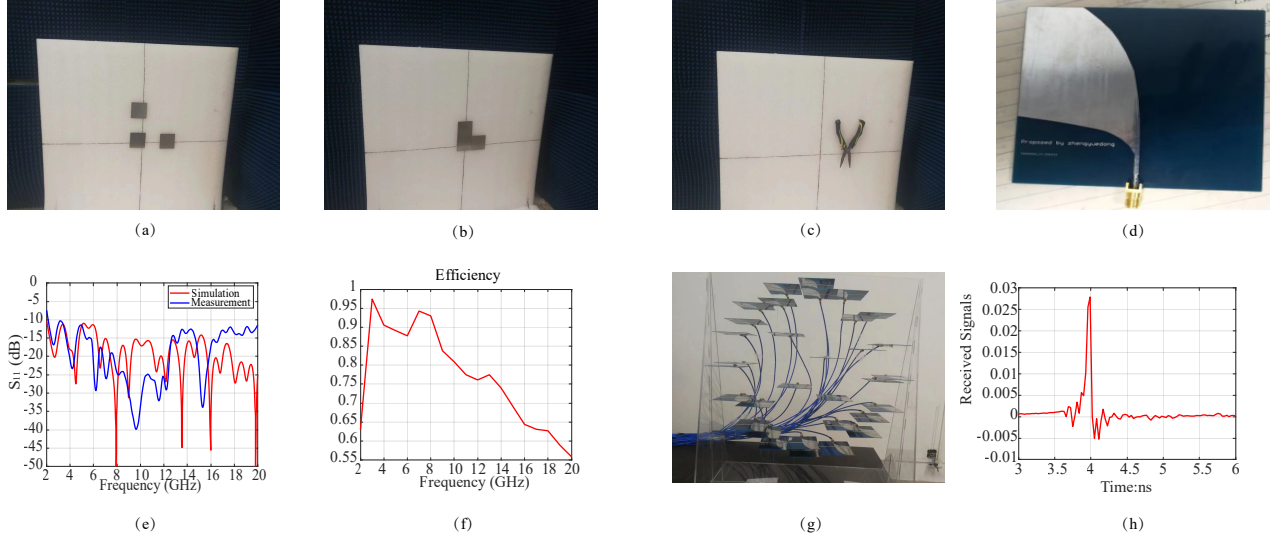
Fig. 12. Measurements of the imaging system in the near-range scenario and the photograph of the objects. (a) The 'L' letter consists of three metallic square pieces. (b) The 'L' letter utilized for resolution test. (c) The pliers. (d) Vivaldi antennas. (e) Return loss (S_{11}) measured with VNA in the anechoic chamber. (f) Antenna radiation efficiency. (g) The proposed 2-D sparse MIMO array. (h) Signal waveforms of the measured reflection from a small metal sphere of 30 mm diameter.

Fig. 13. Experiment results of distributed targets. (a) 2-D and 3-D imaging results of Fig. 12(a) using conventional BP, and (b) using IBPA. (c) 2-D and 3-D imaging results of Fig. 12(b) using conventional BP, and (d) using IBPA. (e) 2-D and 3-D imaging results of Fig. 12(c) using conventional BP, and (f) using IBPA.

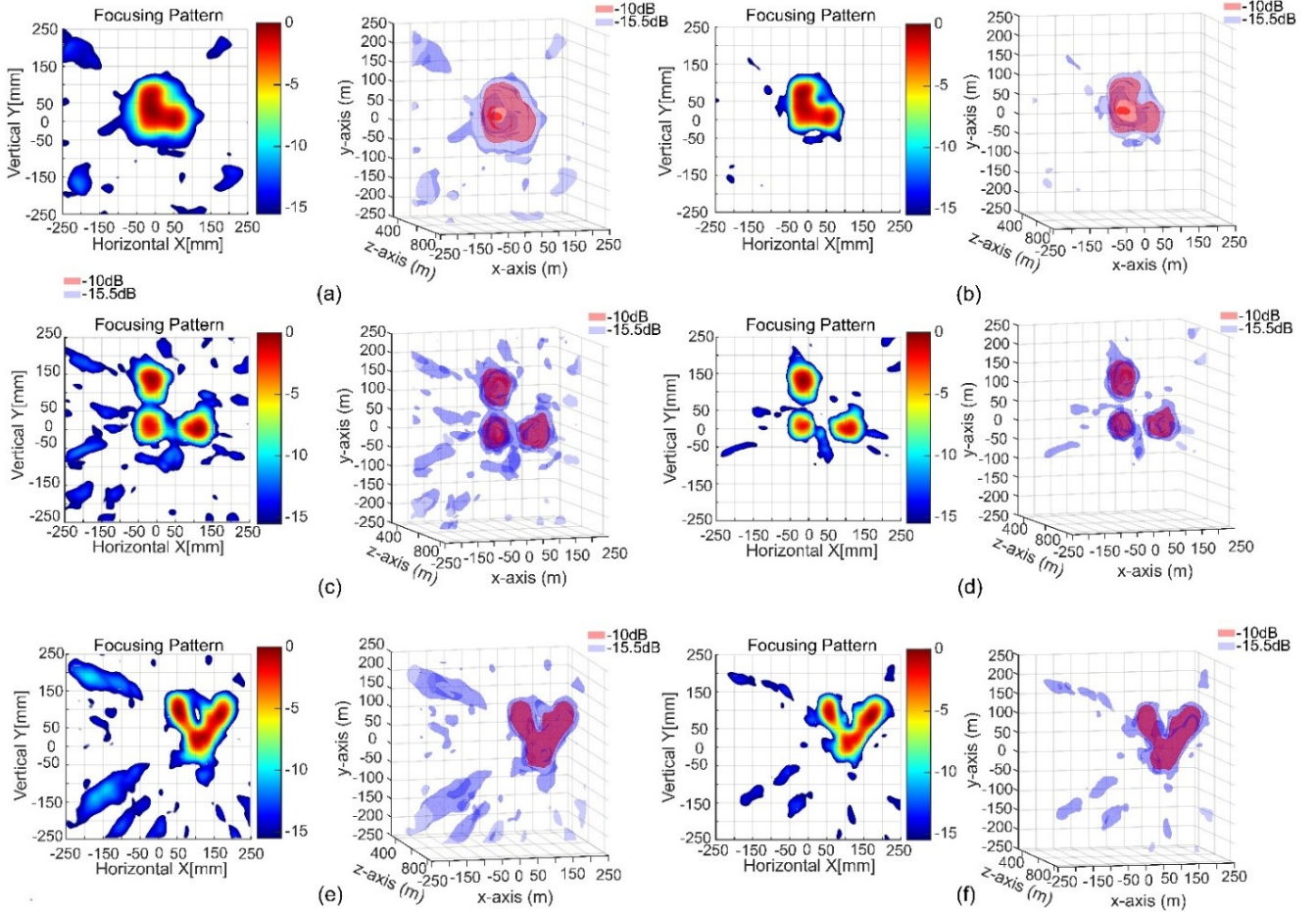of sidelobes 'polluting' the IR region in certain directions. In order to quantitatively evaluate focusing capabilities of above MIMO arrays, the reconstruction error could be defined as,

$$FC = \frac{1}{N} \cdot \sum_{i=1}^{N} \left(f(r_i) - \widehat{f}(r_i) \right)^2 \qquad (23)$$

where $f(\tilde{r_i})$ and $f(r_i)$ are values of the reconstruction image and the ground truth, respectively. N is the number of pixels within the focused image. The quantitative imaging results of using above 2-D MIMO arrays for distributed targets are summarized in Table III. It could be concluded that the proposed array shows the lowest angular properties and the least sidelobes distribution.

In summary, the proposed 2-D sparse MIMO array exhibits a good 3-dB beamwidth and the lowest grating/sidelobe level under the same number of antennas. The simulation results have demonstrated better imaging performance when the proposed 2-D sparse MIMO array is used, which further verifies the effectiveness of the proposed optimization principles.

V. EXPERIMENTAL TESTS AND MEASURED RESULTS

In light of the aforementioned experimental results, the subsequent imaging results will all be compared using the IBPA algorithm. The experimental results of 2-D and 3-D reconstruction images with the proposed array through both IBPA and PSL of -12.74 dB and FC of 7.19 dB^2, thus it has the best conventional BP algorithm have been studied. The experimental measurements are performed in the anechoic chamber. The proposed sparse MIMO array consisting of 16 transmitter and 16 receiver antennas is shown in Fig. 12(g). Vivaldi antennas with an operating bandwidth from 2 to 20 GHz are used as array elements, which are fixed horizontally on an acrylic plate. The gain of antenna within the operational bandwidth is about 8dBi. In order to achieve signal acquisition, all the antennas in the MIMO array are connected to a vector network analyzer (VNA, model Keysight N5234B) through a multi-port RF switch array. The connection sequence of the multi-port RF switch can be effectively controlled by a computer via the host system, enabling automatic switching. The operational bandwidth of the RF switch array ranges from DC to 26.5 GHz and the loss of each channel, s_{21}, is less than 6 dB. The RF output power of VNA is 6 dBm, and the receiver dynamic range is about -118 dB. According to the Friis' transmission equation, we could evaluate the maximum distance with prior knowledge of the vector network analyzer used in the experiment. Beyond this limit, the VNA is unable to extract the echo signal from the background noise. Given the known accuracy of the vector network analyzer, the transmission loss of the imaging system could be calculated as [40],

$$Pr = Pt\,(dBm) + Gt\,(dBi) + Gr\,(dBi)$$
$$+ 20\log_{10}\left(\frac{c}{4\pi}\right) - 20\log_{10}(R) - 20\log_{10}(f) \qquad (24)$$

where f is the operating frequency, R is the distance between transceivers and the target under test. G_t and G_r are the gain of transmitter and receiver elements, respectively. P_t and P_r are the transmitted and received power.

The radar cross section of targets under test within the operational bandwidth is around -30 dBsm. According to (22), the R value is designed from 200 to 895 mm to ensure a good signal to noise ratio (SNR).

Finally, the targets under test are placed in front of the center array at the range of 500 mm, shown in Fig. 13 (a), (b) and (c). 256 spatial measurements of the scattered field reflected from the target could be collected by sequentially switching on and off the corresponding channel of transmitters and receivers. The transmitters are sequentially switched on by the RF switch matrix system and all the transmitters would be executed in a round of testing. When each transmitter is in an active status (on), all receivers would be used to collect the scattered fields from targets.

The operating frequencies of the imaging system range from 5 to 15 GHz with a step of 50 MHz. Hence, 201 frequency samples have been recorded at each pair of the combinations. The background reflections and phase delays caused by the length of corresponding cables, S_{21} and S_{11}, for all transmitter-receiver channels are also measured for calibrations. The reflection signals from a 30mm-diameter metallic ball are measured and illustrated in Fig. 12(h). This is the pulse length mentioned in Principle 1, which affects the sparsity and performance of the array. The product of the speed of propagation c and the pulse duration T determines the element spacing d. When $d \geq cT$, it ensures that the signals from different elements do not overlap in space, thereby avoiding signal interference. In the experiments, three distributed targets shown in Fig. 12(a), (b) and (c) are tested to compare the imaging capabilities of our proposed IBPA and conventional BP algorithm based on the proposed MIMO topology. In Fig. 12(a), the target is a 'L' shaped pattern consisting of three metallic square pieces while Fig. 12(b) is a 'L' letter consisting of three separable metallic square pieces. In Fig. 12(c), the target is a pliers. Fig. 12(e) depicts the measured return loss, S_{11}, of the used Vivaldi antennas, which indicates that the return loss is below -10dB under the whole frequency band of the imaging system. Fig. 12(f) shows the radiation efficiency of the antenna corresponding to its operating frequency band. Both 3-D imaging results and 2-D results, which are obtained by the maximum projections along the down-range direction, are shown in Fig. 13 using both the conventional BP and proposed IBPA methods.

In order to compare the performance of two imaging algorithms, focusing capability FC is utilized. The imaging results of FC and PSL are summarized in Table V. It is shown that the FC got by the proposed IBPA is smaller than the conventional BPA. It is noted in Fig. 13(c) that the metallic pieces are overlapping with each other, which means that the conventional BP almost could not distinguish the adjacent steel pieces. However, the imaging results of three metallic pieces could be clearly recognized with each other in Fig. 13(d). Hence, the proposed IBPA has a much higher cross-range resolution than conventional BPA in IR region.

Besides, the time consumption of the conventional BP and

TABLE V
QUANTITATIVE IMAGING PARAMETERS OF IBPA AND BPA

Objects Under Test	FC		PSL (distributed targets, dB)		CPU time (s)	
	IBPA	BPA	IBPA	BPA	IBPA	BPA
'L' pattern in Fig. 12(a)	9.96	20.8	-13.29	-10.08	510.195	588.143
'L' pattern in Fig. 12(b)	10.23	19.99	-12.81	-11.37	503.599	579.422
Pliers in Fig. 12(c)	10.14	19.44	-12.77	-9.96	491.83	575.8

IBPA methods are illustrated in Table V. All algorithms are implemented in a laptop with a regular 64-bit 3.00-GHz i5-8500 CPU. It is validated that although the better imaging results could be obtained by the proposed IBPA, the higher computational efficiency could be also realized compared to the to conventional BPA.

In summary, the proposed IBPA exhibits better imaging performance than the conventional BP in terms of the PSL level, cross-range resolution and focusing capabilities without increasing the computational complexity.

VI. CONCLUSION

A two-step iterative optimization method for optimal 2-D sparse MIMO planar array topology designs and an improved back-propagation imaging algorithm have been proposed. Extensive simulations and experiments have verified that the proposed MIMO topology has a superior sidelobe-control capability and higher dynamic range (PSL) compared to other topologies, and the IBPA could further improve the imaging performance without increasing the computational complexity. The proposed method could be efficiently applied to any number of elements in a customized aperture size. The IBPA has superiority on dynamic range (PSL level), cross-range resolution, side lobes controlling capability and computational efficiency compared to the conventional BP method. They are promising to industrial non-destructive testing, security imaging, and defense and military fields.

REFERENCES

[1] J. Fu, X. Sun, Z. Wang and K. Fu, "An anchor-free method based on feature balancing and refinement network for multiscale ship detection in SAR images," *IEEE Transactions on Geoscience and Remote Sensing*, vol. 59, no. 2, pp. 1331-1344, Feb. 2021.

[2] S. Li and S. Wu, "Low-cost millimeter wave frequency scanning based synthesis aperture imaging system for concealed weapon detection," *IEEE Transactions on Microwave Theory and Techniques*, vol. 70, no. 7, pp. 3688-3699, July 2022.

[3] A. Zhuravlev, V. Razevig, A. Rogozin and M. Chizh, "Microwave imaging of concealed objects with linear antenna array and optical tracking of the target for high-performance security screening systems," *IEEE Transactions on Microwave Theory and Techniques*, vol. 71, no. 3, pp. 1326-1336, March 2023.

[4] R. Cicchetti, S. Pisa, E. Piuzzi, E. Pittella, P. D'Atanasio and O. Testa, "Numerical and experimental comparison among a new hybrid FT-music technique and existing algorithms for through-the-wall radar imaging," *IEEE Transactions on Microwave Theory and Techniques*, vol. 69, no. 7, pp. 3372-3387, July 2021.

[5] F. H. C. Tivive and A. Bouzerdoum, "Clutter removal in through-the-wall radar imaging using sparse autoencoder with low-rank projection," *IEEE Transactions on Geoscience and Remote Sensing*, vol. 59, no. 2, pp. 1118-1129, Feb. 2021.

[6] M. García-Fernández, G. Álvarez-Narciandi, Y. Álvarez López and F. Las-Heras, "Array-based ground penetrating synthetic aperture radar on board an unmanned aerial vehicle for enhanced buried threats detection," *IEEE Transactions on Geoscience and Remote Sensing*, vol. 61, pp. 1-18, 2023, Art no. 5104218.

[7] Z. -K. Ni, J. Pan, C. Shi, S. Ye, D. Zhao and G. Fang, "DL-based clutter removal in migrated GPR data for detection of buried target," *IEEE Geoscience and Remote Sensing Letters*, vol. 19, pp. 1-5, 2022, Art no. 3507205. (GPR).

[8] B. Wu, Y. Gao, J. Laviada, M. T. Ghasr and R. Zoughi, "Time-reversal SAR imaging for nondestructive testing of circular and cylindrical multilayered dielectric structures," *IEEE Transactions on Instrumentation and Measurement*, vol. 69, no. 5, pp. 2057-2066, May 2020.

[9] C. Liu and R. Zoughi, "Adaptive synthetic aperture radar (SAR) imaging for optimal cross-range resolution and image quality in NDE applications," *IEEE Transactions on Instrumentation and Measurement*, vol. 70, pp. 1-7, 2021.

[10] J. Laviada, B. Wu, M. T. Ghasr and R. Zoughi, "Nondestructive evaluation of microwave-penetrable pipes by synthetic aperture imaging enhanced by full-wave field propagation model," *IEEE Transactions on Instrumentation and Measurement*, vol. 68, no. 4, pp. 1112-1119, April 2019.

[11] A. S. M. Alqadami, A. Zamani, A. Trakic and A. Abbosh, "Flexible electromagnetic cap for three-dimensional electromagnetic head imaging," *IEEE Transactions on Biomedical Engineering*, vol. 68, no. 9, pp. 2880-2891, Sept. 2021.

[12] J. M. Felício, J. M. Bioucas-Dias, J. R. Costa and C. A. Fernandes, "Microwave breast imaging using a dry setup," *IEEE Transactions on Computational Imaging*, vol. 6, pp. 167-180, 2020.

[13] D. Oloumi, R. S. C. Winter, A. Kordzadeh, P. Boulanger and K. Rambabu, "Microwave imaging of breast tumor using time-domain UWB circular-SAR technique," *IEEE Transactions on Medical Imaging*, vol. 39, no. 4, pp. 934-943, April 2020.

[14] Q. Guo, Z. Wang, T. Chang and H. -L. Cui, "Millimeter-wave 3-D imaging testbed with MIMO array," *IEEE Transactions on Microwave Theory and Techniques*, vol. 68, no. 3, pp. 1164-1174, March 2020.

[15] Z. Wang, Q. Guo, X. Tian, T. Chang and H. -L. Cui, "Near-field 3-D millimeter-wave imaging using MIMO RMA with range compensation," *IEEE Transactions on Microwave Theory and Techniques*, vol. 67, no. 3, pp. 1157-1166, March 2019.

[16] M. Kazemi, Z. Kavehvash and M. Shabany, "K-space analysis of aliasing in millimeter-wave imaging systems," *IEEE Transactions on Microwave Theory and Techniques*, vol. 69, no. 3, pp. 1965-1973, March 2021.

[17] A. M. Molaei, S. Hu, V. Skouroliakou, V. Fusco, X. Chen and O. Yurduseven, "Fourier compatible near-field multiple-input multiple-output terahertz imaging with sparse non-uniform apertures," *IEEE Access*, vol. 9, pp. 157278-157294, 2021.

[18] O. T. Von Ramm and S. W. Smith, "Beam steering with linear arrays," *IEEE Trans Biomed. Eng.*, vol. BME-30, no. 8, pp. 438–452, Aug. 1983.

[19] J. Hu, G. Zhu, T. Jin and Z. Zhou, "Grating/side lobes mitigation in sparse UWB MIMO array," *2015 16th International Radar Symposium (IRS)*, Dresden, Germany, 2015, pp. 1070-1075.

[20] W. Zhang et al., "A grating-lobes suppression method for wideband MIMO millimeter-wave imaging arrays," *IEEE Transactions on Antennas and Propagation*, vol. 71, no. 2, pp. 1851-1862, Feb. 2023.

[21] F. Gumbmann and L. -P. Schmidt, "Millimeter-wave imaging with optimized sparse periodic array for short-range applications," *IEEE Transactions on Geoscience and Remote Sensing*, vol. 49, no. 10, pp. 3629-3638, Oct. 2011.

[22] V. Sipal, D. Edwards and B. Allen, "Bandwidth requirement for suppression of grating lobes in ultrawideband antenna arrays," *2012 IEEE*

International Conference on Ultra-Wideband, Syracuse, NY, USA, 2012, pp. 236-240.

[23] X. Zhuge and A. G. Yarovoy, "A sparse aperture MIMO-SAR-Based UWB imaging system for concealed weapon detection," *IEEE Transactions on Geoscience and Remote Sensing*, vol. 49, no. 1, pp. 509-518, Jan. 2011.

[24] K. Tan, S. Wu, Y. Wang, S. Ye, J. Chen and G. Fang, "A novel two-dimensional sparse MIMO array topology for UWB short-range imaging," *IEEE Antennas and Wireless Propagation Letters*, vol. 15, pp. 702-705, 2016.

[25] O. T. Von Ramm, S. W. Smith, and F. L. Thurstone, "Grey scale imaging with complex TGC and transducer arrays," Proc. Soc. Photo-Opt. Inst. Eng., Med. IV, 1975, vol. 70, pp. 266–270.

[26] J. L. Schwartz and B. D. Steinberg, "Ultrasparse, ultrawideband arrays," *IEEE Trans. Ultrason., Ferroelectr. Freq. Control*, vol. 45, no. 2, pp. 376–393, Mar. 1998.

[27] B. D. Steinberg and H. M. Subbaram, *Microwave Imaging Techniques*. New York: Wiley, 1991.

[28] X. Zhuge and A. G. Yarovoy, "Study on two-dimensional sparse MIMO UWB arrays for high resolution near-field imaging," *IEEE Transactions on Antennas and Propagation*, vol. 60, no. 9, pp. 4173-4182, Sept. 2012.

[29] K. Tanet al., "On sparse MIMO planar array topology optimization for UWB near-field high-resolution imaging," *IEEE Transactions on Antennas and Propagation*, vol. 65, no. 2, pp. 989-994, Feb. 2017.

[30] S. Wang, S. Li, A. Hoorfar, K. Miao, G. Zhao and H. Sun, "Compressive sensing based sparse MIMO array synthesis for wideband near-field millimeter-wave imaging," *IEEE Transactions on Aerospace and Electronic Systems*.

[31] X. Zhuge and A. G. Yarovoy, "Sparse multiple-input multiple-output arrays for high-resolution near-field ultra-wideband imaging," *IET Microw., Antennas Propag.*, vol. 5, no. 13, pp. 1552–1562, Oct. 2011.

[32] J. Gao, Y. Qin, B. Deng, H. Wang and X. Li, "Novel efficient 3D short-range imaging algorithms for a scanning 1D-MIMO array," *IEEE Transactions on Image Processing*, vol. 27, no. 7, pp. 3631-3643, July 2018.

[33] A. M. Molaei, S. Hu, V. Skouroliakou, V. Fusco, X. Chen and O. Yurduseven, "Fast processing approach for Near-Field terahertz imaging with linear sparse periodic array," *IEEE Sensors Journal*, vol. 22, no. 5, pp. 4410-4424, 1 March1, 2022.

[34] X. Chen, C. Luo, Q. Yang, L. Yang and H. Wang, "Efficient MMW image reconstruction algorithm based on ADMM framework for Near-Field MIMO-SAR," *IEEE Transactions on Microwave Theory and Techniques*.

[35] J. Gao, B. Deng, Y. Qin, H. Wang and X. Li, "An efficient algorithm for MIMO cylindrical millimeter-wave holographic 3-D imaging," *IEEE Transactions on Microwave Theory and Techniques*, vol. 66, no. 11, pp. 5065-5074, Nov. 2018.

[36] J. Wang, P. Aubry and A. Yarovoy, "3-D short-range imaging with irregular MIMO arrays using NUFFT-Based range migration algorithm," *IEEE Transactions on Geoscience and Remote Sensing*, vol. 58, no. 7, pp. 4730-4742, July 2020.

[37] X. Zhuge, A. G. Yarovoy, T. Savelyev and L. Ligthart, "Modified kirchhoff migration for UWB MIMO array-based radar imaging," *IEEE Transactions on Geoscience and Remote Sensing*, vol. 48, no. 6, pp. 2692-2703, June 2010.

[38] W.A. Schneider, "Integral formulation for migration in two and three dimensions," *Geophysics*, 43, 49-76, 1978.

[39] S. S. Ahmed, A. Schiess and L. -P. Schmidt, "Near field mm-wave imaging with multistatic sparse 2D-arrays," *2009 European Radar Conference (EuRAD)*, Rome, Italy, 2009, pp. 180-183.

[40] H. T. Friis, "A note on a simple transmission formula," *Proceedings of the IRE*, vol. 34, no. 5, pp. 254-256, May 1946.